

Non-classical Electrostriction in Calcium-Doped Cerium Oxide Ceramics

Ahsanul Kabir^{ab}, Victor Buratto Tinti^a, Simone Santucci^a, Maxim Varenik^c, Samuel Griffiths^d, Sebastian Molin^e, Igor Lubomirsky^c, and Vincenzo Esposito^a

a. Department of Energy Conversion and Storage, Technical University of Denmark, Kgs Lyngby 2800, Denmark

b. Institute for Manufacturing Technology of Ceramic Components and Composites, University of Stuttgart, Stuttgart 70569, Germany

c. Department of Molecular Chemistry and Materials Science, Weizmann Institute of Science, Rehovot 7610001, Israel

d. Institute of Materials Science, University of Stuttgart, Stuttgart 70569, Germany

e. Faculty of Electronics, Telecommunications, and Informatics, Gdańsk University of Technology, Gdańsk 80-233, Poland

Email: vies@dtu.dk

1. Materials' structural and microstructural features

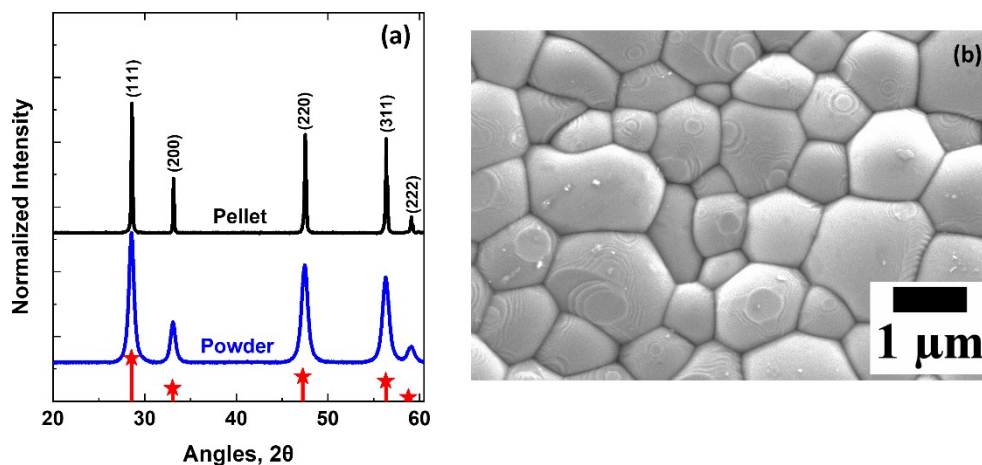


Fig. S1. (a) XRD and (b) SEM image of the GDC-10 ceramics samples, sintered at 1450 °C for 10 hours in air. The XRD pattern is indexed with pure ceria [1].

The diffraction peak is getting broadened for the CDC powder pattern in Fig. 1a. It somewhat shifts towards lower 2θ angles with increasing calcium concentration, leading to the expansion and slight distortion of the crystal lattice structure. The average crystallite size (d) of the

calcined powder is calculated from the Scherrer equation: $d = \frac{0.94\lambda}{\beta \cos\theta}$, where λ is the

wavelength of Cu K α radiation, β is the full width at half-maximum, and θ is Bragg's diffraction angle. The d value is around 50 nm for the CDC-2.5 sample, whereas other compounds have a value between 15-25 nm. The XRD profile for sintered pellets results in narrow and sharp peaks, which indicates high crystallinity due to particle grain growth at high sintering temperatures of 1450 °C for 10 hours.

Table S1. The grain size and lattice constant of the CDC ceramics.

Sample ID	Lattice Constant (Å)	Grain Size (μm)
CDC-2.5	5.4123	4.8 ± 0.3
CDC-5	5.4165	3.5 ± 0.3
CDC-10	5.4174	4.5 ± 0.4
CDC-15	5.418	3.0 ± 0.4

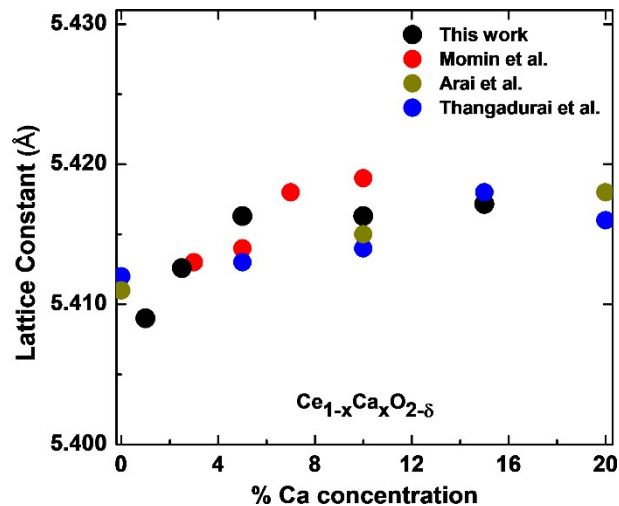


Figure S2: The estimated lattice constant with respect to Ca concentration in $\text{Ce}_{1-x}\text{Ca}_x\text{O}_{2-\delta}$ ceramics, showing an incremental behaviour up to $x = 0.1$. The lattice constant value is compared with the literature data of M. Momin et al. [3], V. Thangadurai et al. [4], and H. Arai et al. [5]. The slight difference is ascribed to the powder synthesis method, starting particle size, sintering conditions, and sample preparation.

The lattice constant did not increase linearly with Ca^{2+} concentration and did not follow Vegard's law. A similar gradual non-linear increment of lattice constant was also reported for $\text{Yb}_x\text{Ce}_{1-x}\text{O}_{2-\delta}$, $\text{Nd}_x\text{Ce}_{1-x}\text{O}_{2-\delta}$, and $\text{Y}_x\text{Ce}_{1-x}\text{O}_{2-\delta}$ systems [6][7].

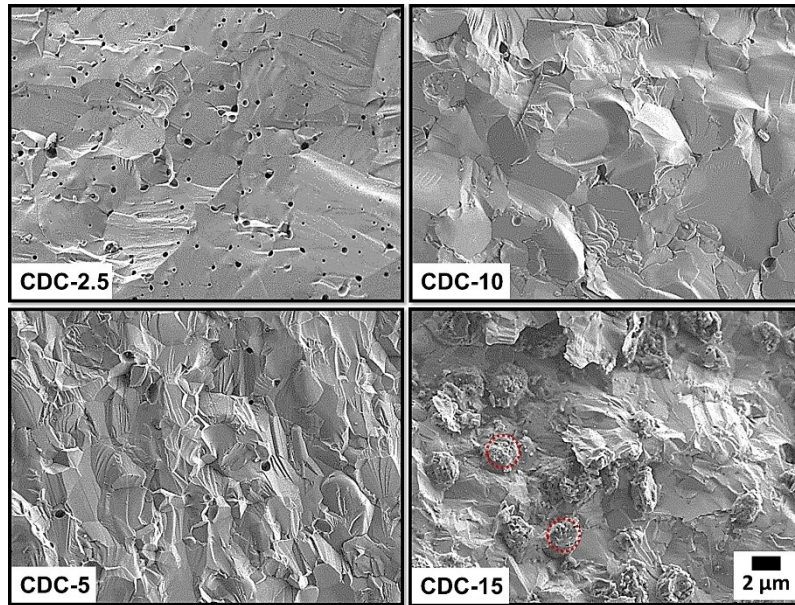


Fig. S3: SEM images of the cold-fractured phase of the dense CDC ceramics samples.

The bulk density of the sintered samples was measured using the Archimedes method, above 95% of the theoretical density. As observed in **Fig. S3**, the microstructure is dense and in line with the experimental density values. Only the CDC-2.5 sample shows a small percentage of intergranular pores. As assessed via the linear intercept method, the number-average grain size ranges between 3-5 μm (**Table S1**). The red circles in the CDC-15 sample confirm the presence of a secondary phase. An earlier publication reported a similar result, showing no composition variation within the segregated zone [2].

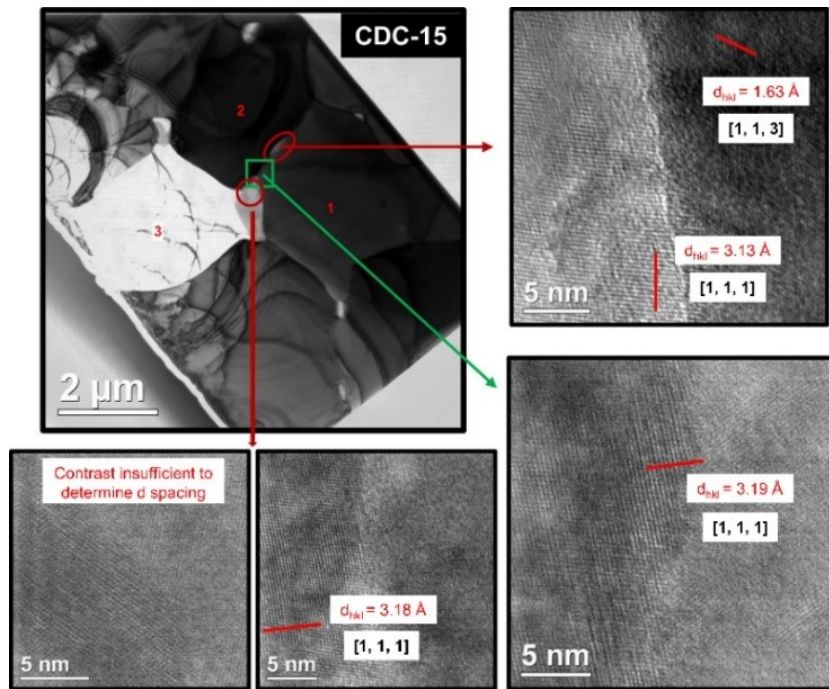


Fig. S4: A typical bright-field TEM image and characteristic Fast Fourier Transformation (FFT) images of the CDC-15 sample. The white region represents the grain boundary triple junction. The interplanar d spacing value is about ~ 3.15 Å and 1.63 Å for [111] and [113] planes.

2. Mechanical properties

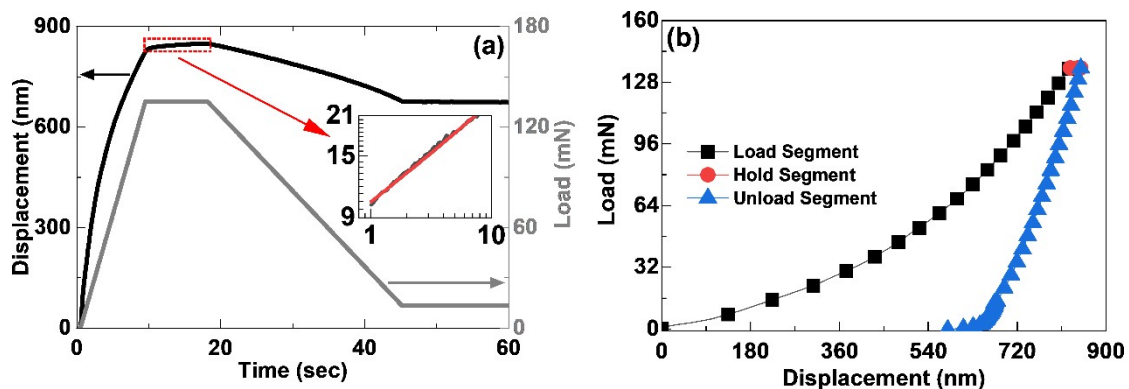


Fig. S5: (a) A typical displacement/load–time curve in the fast nanoindentation measurement for CDC-5 samples at room temperatures. The inset illustrates the displacement under a constant hold segment, showing a primary creep response. (b) The load-displacement curve shows an increment of displacement at maximum load.

The mechanical properties of CDC ceramics samples were measured via the nanoindentation (NI) and ultrasound pulse-echo velocity (SV) method at room temperature. The nanoindentation depth is well formed, and no pop-ups or instabilities were observed during the

measurements. Likewise, in rare-earth doped ceria compounds [8], all CDC ceramics exhibit noticeable primary creep during the load-hold phase in the NI measurement (see **Fig. S5**). The creep constant (A) was estimated from the time-displacement curve that follows the relation $\Delta u = A (\Delta t)^{1/3}$, where Δu and Δt are the change of displacement and time, respectively, at constant loading [9].

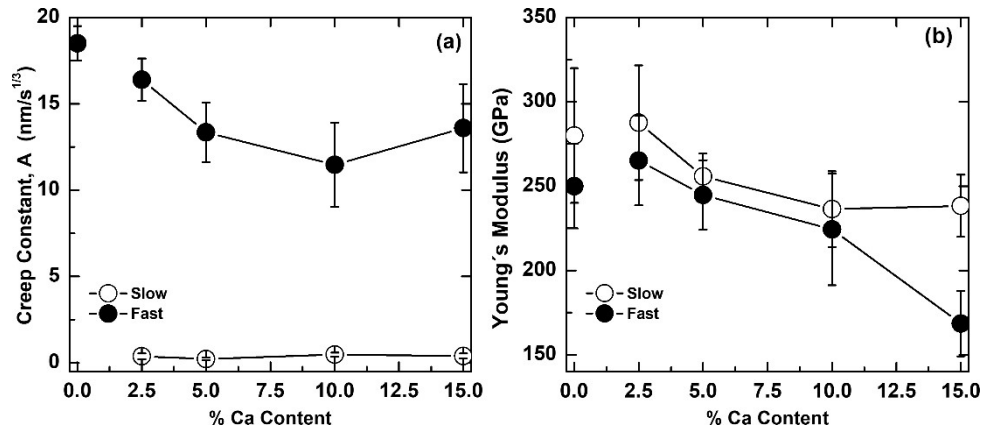


Fig. S6: Room temperature (a) creep constant and (b) Young's modulus of calcium-doped ceria ceramics as a function of dopant concentration under fast and slow loading, with a maximum load of 150 mN. The creep constant (Fast) and Young's modulus value of undoped ceria are taken from Korobko et al. [9] and Varenik et al., [10], respectively.

As can be seen in **Fig. S6a**, a large difference in creep rate constant (A) occurs between the fast (15 mN/s) and slow (0.15 mN/s) load conditions, which meaningfully underlines the effect of the load speed on creep magnitude. The origin of the creep mechanism in cerium oxide is attributed to the time-dependent lattice complex ($7O-Ce_{Ce}-\dot{V}_O$) reorientation under the anisotropic mechanical stress field [8][11]. As the lattice response is time-dependent, at fast loading, i.e., the time required for lattice reorientation is higher than the given load rate. Accordingly, the lattice rearranges during the load-hold phase, leading to creep deformation. Whereas at slow loading, the time scale for loading is considerably slow concerning lattice reorganization time, resulting in a reduction of deformation during the hold phase. It is interesting to note that creep is suppressed with calcium concentration (an increase in the \dot{V}_O concentration) for $0.025 < x < 0.1$. This observance agrees with the previous experimental result, suggesting that increased oxygen vacancy concentration accelerates point defect rearrangement, alleviating the indenter's mechanical pressure [11]. However, increased A value at higher doping, e.g., CDC-15, is due to the formation of the excessive dopant-vacancy cluster and a possible transition of fluorite to a double fluorite structure. Considering the indentation depth (700-800 nm) and the grain size of the materials, it is highly expected that the grain boundaries insignificantly influence creep. Compared to CDC compounds, the GDC-10

compound has a reported creep constant value of $18 \text{ nm/s}^{1/3}$, obtained using a similar methodology (rapid loading) [12][13]. This result indicates that the CDC is less anelastic than the GDC. As expected, the creep behavior affects Young's modulus derived from NI (**Fig. S6b**), revealing considerable differences between fast and slow modes. More specifically, a large deviation is observed for CDC-15. The magnitude of Young's modulus in slow measurement is approximately 15-70 GPa higher than in fast mode, depending on the dopant content. Young's modulus shows a declining trend with calcium concentration agreeing with the theoretical prediction since the dopant (Ca) increases the average bond length. i.e., lattice constant, and reduces the chemical bond number [14]. On the contrary, the early work of Yan et al. [15] shows that calcium-doped ceria does not demonstrate considerable change in Young's modulus concerning Ca concentration. These authors emphasized that CDC undergoes phase segregation and has to be viewed as a composite of Ca-rich and Ca-poor phases. Young's modulus of GDC-10 is 210 GPa, measured in fast loading mode [7][12].

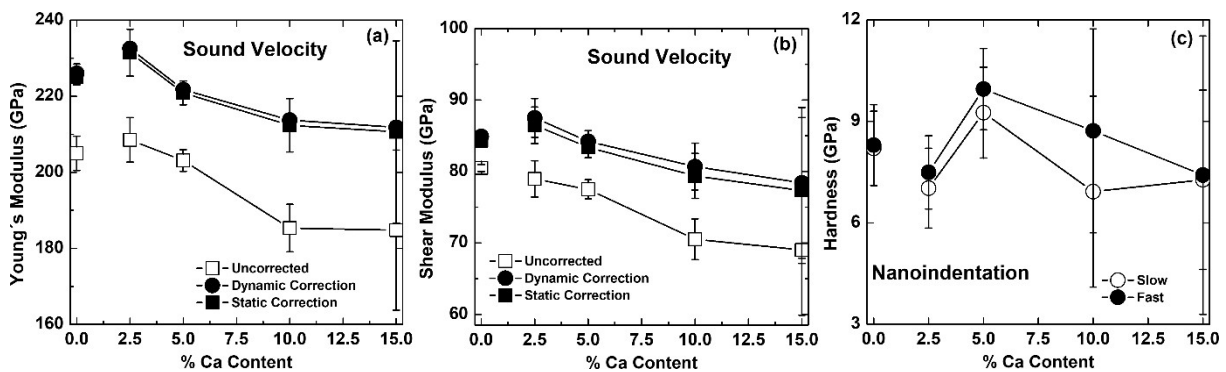


Fig. S7: Uncorrected and porosity-corrected (a) Young's and (b) shear modulus, as calculated from sound velocity (SV) measurements, and (c) Hardness estimated from the nanoindentation method of the CDC ceramics. The data of undoped ceria is taken from Varenik et al. [10].

The longitudinal and shear sound velocities were measured with accuracy better than 0.25% from pellet height, and the ultrasound time of flight was measured using a transducer attached to the pellets with high viscosity commercial honey without additional force, as described in [10][16]. The two models, static and dynamic, are explained in detail in the Supplementary file of Ref. [10]. The mechanical properties results, as determined by sound velocity (SV) measurements, are revealed in **Fig. S7**, highlighting the absence of microcracks in the samples. As expected, the shear and Young's moduli monotonically decrease with calcium concentration. Moreover, Young's modulus calculated from SV measurements is slightly smaller than NI's. The nano hardness value is higher in the fast measurement than in the slow

one. However, the calcium dependency on the hardness value cannot be confirmed because of the large statistical uncertainty in the CDC-10 and CDC-15 samples.

3. Electrochemical properties

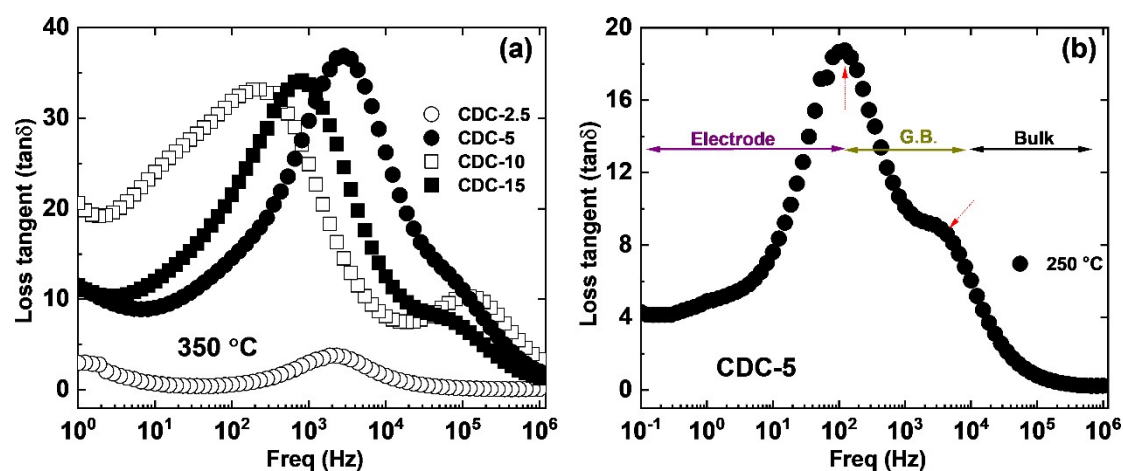


Fig. S8: (a) Comparison of frequency-dependent dielectric loss tangent of the CDC samples at 350 °C. (b) Frequency-dependent dielectric loss tangent plot at 250 °C for the CDC-5 compound, illustrating two relaxation peaks associated with grain interior (bulk) and grain boundary.

Table S2. The capacitance and relaxation frequency of the CDC samples at 300 °C.

Sample ID	C_{bulk} (F)	$C_{\text{g.b.}}$ (F)	f_{bulk} (Hz)	$f_{\text{g.b.}}$ (Hz)
CDC-2.5	$1.5 \cdot 10^{-11}$			$3.0 \cdot 10^3$
CDC-5	$2.8 \cdot 10^{-11}$	$5.5 \cdot 10^{-09}$	$40 \cdot 10^4$	$10 \cdot 10^3$
CDC-10	$3.0 \cdot 10^{-11}$	$2.2 \cdot 10^{-08}$	$50 \cdot 10^4$	$3.0 \cdot 10^3$
CDC-15	$2.5 \cdot 10^{-11}$	$4.5 \cdot 10^{-09}$	$35 \cdot 10^4$	$5.5 \cdot 10^3$

Fig. S9a displays the characteristic impedance plot, i.e., Nyquist plot (ρ' vs ρ'' characterized by frequency) of CDC samples, examined at 300 °C. The impedance data were fit with an equivalent circuit model, comprising a series of RQ subcircuits, where R and Q correspondingly denoted as the resistor and constant phase element. As noticed, all investigated samples, excluding CDC-2.5, reveal two well-defined semicircles at high and intermediate frequencies, respectively, attributed to bulk (grain) and grain boundary polarization according to the brick-layer model. The low-frequency arc (tailed feature) is associated with the electrode-electrolyte interface, expressing a partial non-blocking behaviour. In this work, the electrode effect is not relevant for further discussion. As evidenced in **Fig. S9a**, the CDC-5 and CDC-10 duo exhibit comparable bulk resistivity, whereas roughly twofold larger resistivity is estimated in the CDC-15 sample. Moreover, they display distinct grain boundary resistivity.

The blocking barrier effect on charge transport is characterized by the grain boundary blocking

factor ($\alpha_{g.b.}$) where $\alpha_{g.b.} = \frac{R_{g.b.}}{R_{bulk} + R_{g.b.}}$ [17]. The estimated $\alpha_{g.b.}$ is in a non-blocking nature

in the materials. The $\alpha_{g.b.} \sim 0.35$ for CDC-10 is considerably higher than of the CDC-15 sample

($\alpha_{g.b.} \sim 0.2$). However, this outcome does not agree with the microstructure analysis, as CDC-

15 displays strong local segregation of calcium at the grain boundaries/triple points. Such a

difference highlights that the ion-blocking effect is not a mere geometrical parameter of grain

but attributed to the solute drag effect during diffusion, accounting for the combined

contribution from the purity of the starting powders, dopant segregation, nanodomains

formation, microcracks, etc. For the case of the CDC-2.5 sample, a single semicircle is

observed, corresponding to overlapped bulk and grain boundary contribution. Accordingly, the

blocking effect cannot be distinguished, and only the total resistivity is assessed. As expected,

with the rise of temperature, the impedance response moves towards the origin, i.e., a decrease

of resistance (R). From the impedance data, bulk/grain, grain boundary, and total ionic

conductivity are estimated and shown in **Fig. S9b-d** as a function of temperature. The bulk

conductivity (σ_{∞}) is calculated with the following formula, $\sigma_{\infty} = \frac{1}{R_{\infty}A} \frac{t}{A}$, where t is the pellet

thickness, and A is the electrode area. R_{∞} denotes the bulk resistance. The grain boundary

conductivity ($\sigma_{g.b.}$) is computed using the formula, $\sigma_{g.b.} = \left(\frac{\tau_{\infty}}{\tau_{g.b.}}\right) \sigma_{\infty}$, assuming that the

dielectric constant of the bulk and grain boundary is identical. τ is the relaxation time,

$\tau = RC = \frac{1}{2\pi f}$ where f is the frequency. The activation energy of charge migration for bulk and

grain boundary is reported respectively as ~ 0.85 and ~ 1.10 eV, underlining no substantial

variation with the response to nominal calcium concentration. The startling conclusion is that

the secondary CaO_x phase, thought to be an isolating phase, does not impact the total ionic

conductivity. The total conductivity is significantly low in the CDC-2.5 sample, whereas the

other compositions illustrate a similar value analogous to the reference GDC-10 sample. A

single activation energy furthermore highlights that no change of charge transport pathway

associated with oxygen vacancies as a function of temperature is observed [18].

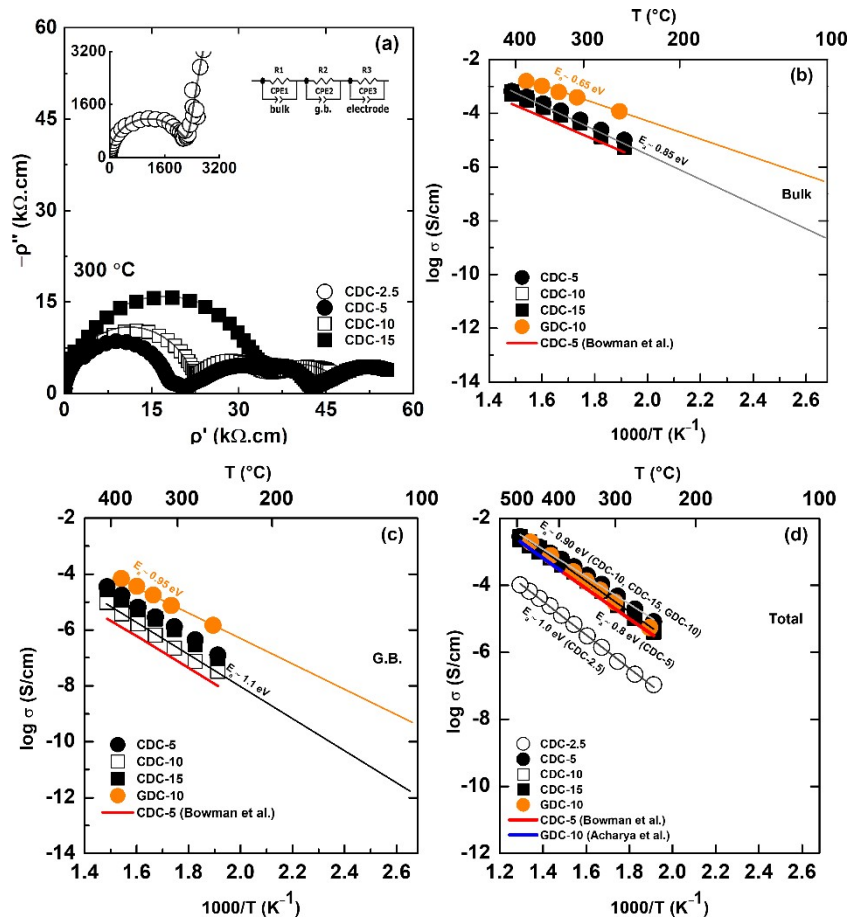


Figure S9: (a) Illustration of typical geometry normalized Nyquist plots (ρ' vs ρ'') of CDC ceramics at 300 °C, measured in ambient air. The distinct arcs refer to the impedance responses of bulk/grain and grain boundary and electrode. The temperature-dependent Arrhenius plots of (b) bulk, (c) grain boundary, and (d) total electrical conductivities of the CDC ceramics. Note that grain boundary conductivity is the effective conductivity of a single-grain boundary. The reference CDC-5 and GDC-10 data is taken from Ref. [19] and Ref. [20].

References:

- [1] A. Kabir *et al.*, "Effect of oxygen defects blocking barriers on gadolinium doped ceria (GDC) electro-chemo-mechanical properties," *Acta Mater*, vol. 174, pp. 53–60, Aug. 2019, doi: 10.1016/j.actamat.2019.05.009.
- [2] M. YAN, T. MORI, J. ZOU, F. YE, D. OU, and J. DRENNAN, "TEM and XPS analysis of $\text{Ca}_x\text{Ce}_{1-x}\text{O}_{2-y}$ ($x=0.05-0.5$) as electrolyte materials for solid oxide fuel cells," *Acta Mater*, vol. 57, no. 3, pp. 722–731, Feb. 2009, doi: 10.1016/j.actamat.2008.10.014.
- [3] N. Momin, J. Manjanna, S. Kobayashi, S. T. Aruna, S. Senthil Kumar, and G. P. Nayaka, "Synthesis and ionic conductivity of calcium-doped ceria relevant to solid oxide fuel cell applications," *Mater Adv*, vol. 3, no. 23, pp. 8780–8791, 2022, doi: 10.1039/D2MA00868H.
- [4] V. Thangadurai and P. Kopp, "Chemical synthesis of Ca-doped CeO_2 —Intermediate temperature oxide ion electrolytes," *J Power Sources*, vol. 168, no. 1, pp. 178–183, May 2007, doi: 10.1016/j.jpowsour.2007.03.030.

- [5] H. Arai, "Electrical properties of calcia-doped ceria with oxygen ion conduction," *Solid State Ion*, vol. 20, no. 4, pp. 241–248, Jul. 1986, doi: 10.1016/0167-2738(86)90041-X.
- [6] I. STEPHENS and J. KILNER, "Ionic conductivity of $Ce_{1-x}Nd_xO_{2-x/2}$," *Solid State Ion*, vol. 177, no. 7–8, pp. 669–676, Mar. 2006, doi: 10.1016/j.ssi.2006.01.010.
- [7] S. OMAR, E. WACHSMAN, and J. NINO, "Higher conductivity Sm^{3+} and Nd^{3+} co-doped ceria-based electrolyte materials," *Solid State Ion*, vol. 178, no. 37–38, pp. 1890–1897, Feb. 2008, doi: 10.1016/j.ssi.2007.12.069.
- [8] E. Wachtel, A. I. Frenkel, and I. Lubomirsky, "Anelastic and Electromechanical Properties of Doped and Reduced Ceria," *Advanced Materials*, vol. 30, no. 41, p. 1707455, Oct. 2018, doi: 10.1002/adma.201707455.
- [9] R. Korobko *et al.*, "Influence of Gd content on the room temperature mechanical properties of Gd-doped ceria," *Scr Mater*, vol. 66, no. 3–4, pp. 155–158, Feb. 2012, doi: 10.1016/j.scriptamat.2011.10.027.
- [10] M. Varenik, S. Cohen, E. Wachtel, A. I. Frenkel, J. C. Nino, and I. Lubomirsky, "Oxygen vacancy ordering and viscoelastic mechanical properties of doped ceria ceramics," *Scr Mater*, vol. 163, pp. 19–23, Apr. 2019, doi: 10.1016/j.scriptamat.2018.12.024.
- [11] R. Korobko, S. K. Kim, S. Kim, S. R. Cohen, E. Wachtel, and I. Lubomirsky, "The role of point defects in the mechanical behavior of doped ceria probed by nanoindentation," *Adv Funct Mater*, 2013, doi: 10.1002/adfm.201301536.
- [12] A. Kabir, J. Kyu Han, B. Merle, and V. Esposito, "The role of oxygen defects on the electro-chemo-mechanical properties of highly defective gadolinium doped ceria," *Mater Lett*, vol. 266, p. 127490, May 2020, doi: 10.1016/j.matlet.2020.127490.
- [13] A. Kabir *et al.*, "Effect of cold sintering process (CSP) on the electro-chemo-mechanical properties of Gd-doped ceria (GDC)," *J Eur Ceram Soc*, vol. 40, no. 15, pp. 5612–5618, Dec. 2020, doi: 10.1016/j.jeurceramsoc.2020.06.010.
- [14] Y. WANG, K. DUNCAN, E. WACHSMAN, and F. EBRAHIMI, "The effect of oxygen vacancy concentration on the elastic modulus of fluorite-structured oxides," *Solid State Ion*, vol. 178, no. 1–2, pp. 53–58, Jan. 2007, doi: 10.1016/j.ssi.2006.11.003.
- [15] M. Yan, T. Mori, J. Zou, H. Huang, and J. Drennan, "Microstructures and mechanical properties of $Ce_{1-x}Ca_xO_{2-y}$ ($x=0.05, 0.1, 0.2$) with different sintering temperatures," *J Eur Ceram Soc*, vol. 30, no. 3, pp. 669–675, Feb. 2010, doi: 10.1016/j.jeurceramsoc.2009.09.005.
- [16] O. Yeheskel and O. Tevet, "Elastic Moduli of Transparent Yttria," *Journal of the American Ceramic Society*, vol. 82, no. 1, pp. 136–144, Dec. 2004, doi: 10.1111/j.1151-2916.1999.tb01733.x.
- [17] K. Neuhaus, R. Dolle, and H.-D. Wiemhöfer, "Assessment of the Effect of Transition Metal Oxide Addition on the Conductivity of Commercial Gd-Doped Ceria," *J Electrochem Soc*, 2018, doi: 10.1149/2.1111807jes.

- [18] S. Banerjee, P. S. Devi, D. Topwal, S. Mandal, and K. Menon, "Enhanced ionic conductivity in Ce_{0.8}Sm_{0.2}O_{1.9}: Unique effect of calcium Co-doping," *Adv Funct Mater*, 2007, doi: 10.1002/adfm.200600890.
- [19] W. J. Bowman, M. N. Kelly, G. S. Rohrer, C. A. Hernandez, and P. A. Crozier, "Enhanced ionic conductivity in electroceramics by nanoscale enrichment of grain boundaries with high solute concentration," *Nanoscale*, vol. 9, no. 44, pp. 17293–17302, 2017, doi: 10.1039/C7NR06941C.
- [20] S. A. Acharya, V. M. Gaikwad, V. Sathe, and S. K. Kulkarni, "Influence of gadolinium doping on the structure and defects of ceria under fuel cell operating temperature," *Appl Phys Lett*, vol. 104, no. 11, Mar. 2014, doi: 10.1063/1.4869116.